Gilbert damping in NiFeGd compounds: Ferromagnetic resonance versus time-resolved spectroscopy

R. Salikhov,[1,2,*] A. Alekhin,[3] T. Parpiiev,[3] T. Pezeril,[3] D. Makarov,[4] R. Abrudan,[2,5] R. Meckenstock,[1] F. Radu,[5] M. Farle,[1] H. Zabel,[2] and V. V. Temnov[1,3,†]

[1]*Faculty of Physics and Center for Nanointegration (CENIDE), University of Duisburg-Essen, 47057 Duisburg, Germany*

[2]*Institute for Condensed Matter Physics, Ruhr-University Bochum, 44780 Bochum, Germany*

[3]*Institute of Molecules and Materials of Le Mans, CNRS UMR 6283, 72085 Le Mans, France*

[4]*Helmholtz-Zentrum Dresden-Rossendorf e.V., Institute of Ion Beam Physics and Materials Research, Bautzner Landstrasse 400, 01328 Dresden, Germany*

[5]*Helmholtz-Zentrum Berlin für Materialien und Energien, Albert-Einstein-Strasse 15, 12489 Berlin, Germany*

(Received 19 September 2018; revised manuscript received 14 January 2019; published 11 March 2019)

Engineering the magnetic properties (Gilbert damping, saturation magnetization, exchange stiffness, and magnetic anisotropy) of multicomponent magnetic compounds plays a key role in fundamental magnetism and its applications. Here, we perform a systematic study of $(Ni_{81}Fe_{19})_{100-x}Gd_x$ films with $x = 0\%$, 5%, 9%, and 13% using ferromagnetic resonance (FMR), element-specific time-resolved x-ray magnetic resonance, and femtosecond time-resolved magneto-optical pump-probe techniques. The comparative analysis of field and time domain FMR methods, with complimentary information extracted from the dynamics of high-frequency exchange magnons in ferromagnetic thin films, is used to investigate the dependence of Gilbert damping on the Gd concentration.

DOI: 10.1103/PhysRevB.99.104412

I. INTRODUCTION

Ferromagnetic resonance (FMR) spectroscopy is a powerful method for the characterization of magnetic properties in ferromagnetic films and multilayers [1–3]. It is sensitive to the effective magnetization originating from an interplay of the shape anisotropy and perpendicular anisotropy, which usually oppose each other [1,2,4]. Aside from magnetic anisotropy, FMR allows us to derive the spectroscopic splitting g factor, representing the admixture of the orbital contribution to the total magnetic moment [2,5] and the magnetic relaxation [1,2]. Recording spin wave higher harmonics by the resonance absorption provides a quantitative estimate of the magnetic exchange stiffness [6,7]. Nowadays, there is a plethora of methods for the detection of resonant magnetization dynamics in ferromagnetic thin-film systems. Among them, pump-probe techniques with laser pulse or electrical field (pump) excitation and optical or x-ray light (probe) detection play a significant role in the characterization of magnetic dynamical properties in thin-film heterostructures [7–10]. These techniques provide possibilities to detect high-frequency (up to terahertz) magnetization precession and element-selective magnetization dynamics if a synchrotron light is used [10]. The stroboscopic methods show very good agreement with conventional cavity-based FMR spectrometry in determining the resonance frequencies and fields [8,11]. This is not surprising since the Landau-Lifshitz-Gilbert (LLG) equation describes phenomenologically the magnetization dynamics regardless of the excitation method. The LLG equation can be written as [1]

$$\frac{d\mathbf{M}}{dt} = -\gamma\mu_0[M \times H_{\text{eff}}] + \frac{\alpha}{M_s}\left[\mathbf{M} \times \frac{d\mathbf{M}}{dt}\right], \tag{1}$$

where $\gamma = g\mu_B/\hbar$ is the absolute value of the electron gyromagnetic ratio, g is the spectroscopic splitting factor, $\hbar$ is the Planck constant, μ_B is the Bohr magneton, and M_s is the saturation magnetization. The first term in Eq. (1) describes the precession of the magnetization in the effective magnetic field H_{eff}, which includes the external magnetic field, the demagnetizing field, the magnetocrystalline anisotropy field, and the excitation field. The second term represents the "damping torque" proportional to the magnetization precession rate (viscous damping). The dimensionless Gilbert damping parameter is denoted by α [1,2].

The magnetic damping parameter α can be determined from the frequency dependence of the FMR linewidth using conventional FMR techniques [1,2,12]. Time-resolved methods, implying pump-probe techniques, usually record the evolution of the magnetization vector projection after excitation by an ultrashort laser pulse. Thus, time-resolved measurements provide the decay time τ or the relaxation frequency, i.e., the rate at which the precessing magnetization returns to its equilibrium position. In the case of a homogeneous excitation (uniform FMR mode) and $\alpha \ll 1$ (underdamped oscillator), the precessional dynamics is described by the following equation:

$$\phi(t) = \phi_0 \exp(-t/\tau)\sin(\omega t + \varphi_0), \tag{2}$$

*ruslan.salikhov@uni-due.de

†vasily.temnov@univ-lemans.fr

where the parameter $\phi(t)$ is proportional to the angle between the magnetization vector and its equilibrium direction, τ is the characteristic decay time of the magnetization precession, and $f = \omega/2\pi$ is the FMR precessional frequency. The oscillation amplitude ϕ_0 and phase φ_0 usually serve as free parameters [13,14]. The experimentally determined relaxation time τ usually incorporates the inhomogeneous dephasing of FMR oscillators in the investigated sample, resulting in a larger *effective* Gilbert damping $\alpha_{\text{eff}} > \alpha$.

In thin ferromagnetic films both the relaxation rate $1/\tau$ and the resonance frequency ω depend on the amplitude and orientation of the external magnetic field H. For the magnetic field perpendicular to the film plane the relationship between ω and τ is given by [1,2]

$$1/\tau = \alpha_{\text{eff}}\omega = \alpha_{\text{eff}}\gamma\mu_0(H - M_{\text{eff}}), \tag{3}$$

with $\omega = \gamma\mu_0(H - M_{\text{eff}})$ and the effective magnetization

$$M_{\text{eff}} = M_s - \frac{2K_{2\perp}}{\mu_0 M_s}, \tag{4}$$

where $K_{2\perp}$ accounts for the perpendicular magnetic anisotropy. The relationship for an in-plane magnetic field

$$1/\tau = \alpha_{\text{eff}}\sqrt{\omega^2 + \left(\frac{\gamma\mu_0 M_{\text{eff}}}{2}\right)^2} = \alpha_{\text{eff}}\gamma\mu_0\left(H + \frac{M_{\text{eff}}}{2}\right) \tag{5}$$

is obtained using the Kittel expression for the FMR frequency in the parallel configuration:

$$\omega = \gamma\mu_0\sqrt{H(H + M_{\text{eff}})}. \tag{6}$$

Thus, the amplitude and orientation of the external magnetic field play a crucial role for extracting the effective Gilbert damping parameter α_{eff} from the frequency dependence of the relaxation rate $1/\tau(\omega)$.

However, there exists a gap between conventional FMR measurements [1,2] and the dynamic measurements monitoring the complex spatiotemporal transients in ferromagnets induced by ultrashort laser pulses [7–9]. Apart from the general scientific interest in the understanding of ultrafast magnetization dynamics in generic ferromagnetic materials at femtosecond to nanosecond timescales, the particular class of antiferromagnetically coupled rare-earth-transition-metal (RE-TM) alloys deserves special attention. In particular, we refer to the discovery of the phenomenon of ultrafast all-optical magnetization switching in ferrimagnetic RE-TM alloys driven by both ultrashort circularly polarized laser pulses [15] and purely thermal stimuli not assisted by the transfer of the angular momentum from excitation pulses [16,17]. Although the microscopic mechanism responsible for the magnetic switching in RE-TM alloys is still being intensively debated [18], it has been agreed that a necessary condition for the all-optical switching is the presence of two antiferromagnetically coupled magnetic sublattices, which demagnetize on noticeably different timescales after laser-induced heating. It has been shown experimentally that in the amorphous ferrimagnetic GdFeCo alloy the characteristic demagnetizing time for the Fe moment is by a factor of 4 shorter than that for the Gd magnetic moments [16]. This difference is attributed to different magnetic moments ($2.4\mu_B$ for Fe versus $7.9\ \mu_B$ for Gd). The scaling of the demagnetization time with the atomic magnetic moment indicates that the dominant demagnetization process is the thermal noise from the Langevin dynamics [16–21].

Irrespective of the microscopic origin of the nonequilibrium ultrafast demagnetization process, it is expected to be linked to Gilbert damping α [19,20]. Moreover, in the case of the film thickness exceeding the optical skin depth, the spatially inhomogeneous demagnetization and changes in local magnetocrystalline anisotropy [8] trigger the precessional dynamics of spatially homogeneous (FMR) and inhomogeneous standing spin wave modes denoted as *exchange magnons* throughout this paper.

Using a series of Gd-doped permalloy ($Ni_{81}Fe_{19}$) films, we report a comprehensive study of their magnetic properties extracted from conventional FMR measurements and stroboscopic techniques, namely, time-resolved x-ray resonant magnetic scattering (TR-XRMS) [22–25] and the time-resolved magneto-optical Kerr effect (TR-MOKE) [7,8]. The systematic study of Gd-doped permalloy (Py) samples with different Gd concentrations (0, 5, 9, and 13 at %) allows us to compare the accuracy of the values of the intrinsic magnetic damping parameter α, derived using different experimental techniques. The possible contribution of sample imperfections (quality of interfaces and roughness) to the magnetic relaxation, known as a local resonance [26], will be discussed. Furthermore, the Gilbert damping parameter α extracted from the decay time of exchange magnons provides a qualitatively similar dependence on the Gd concentration.

II. EXPERIMENTAL METHODS

$Py_{100-x}Gd_x$ films were grown using magnetron sputter deposition with a base pressure of 3×10^{-8} mbar. Permalloy samples with varying Gd concentration were grown at room temperature by cosputtering $Ni_{81}Fe_{19}$ and Gd at an Ar gas pressure of 1.5×10^{-3} mbar. Sapphire (Al_2O_3) *a*-plane substrates covered by a 5-nm-thick Ta adhesion layer were used for the sample preparation. Prior to Py and Gd sputtering, a 50-nm-thick Cu layer was deposited on top of Ta. The Cu layer serves as a conductor for electrical current pulses in TR-XRMS experiments described elsewhere [22–24,27,28]. All samples were capped by a 5-nm-thick Ta layer for protection against oxidation. All $Py_{100-x}Gd_x$ layers have a total thickness of about 50 nm. The samples have the following layer sequence and composition: Al_2O_3 (substrate)/Ta/Cu/$Py_{100-x}Gd_x$/Ta, where $x = 0\%$, $(5 \pm 1)\%$, $(9 \pm 1)\%$ and $(13 \pm 1)\%$. The concentration of Gd dopants was calculated from sputtering rates of Py and Gd; error bars are determined by uncertainties in the growth rates. The Py deposition rate of 0.1 nm/s at an Ar gas pressure of 1.5×10^{-3} mbar was fixed for all samples. Gd deposition rates of 0.014, 0.026, and 0.039 nm/s were used to achieve 5, 9, and 13 at % of Gd concentration in Py, respectively. The deposition rates for Py and Gd were checked prior to preparation of each sample using a calibrated quartz thickness monitor. During the growth the sample holder was rotated at 1 Hz to ensure homogeneity of the films. All samples were grown under a magnetic field of about 200 mT applied parallel to the substrate plane. The growth under the static bias field resulted in a small in-plane uniaxial magnetic anisotropy of

approximately 0.3 mT for all magnetic films. This induced uniaxial anisotropy helped to maintain Py films in a magnetically homogeneous state at small magnetic fields for the TR-XRMS measurements.

Structural quality of the samples was characterized by x-ray diffraction (XRD) using a Cu K_α radiation source. The FMR spectra were recorded using a conventional Bruker X-band FMR spectrometer operated at a microwave frequency of 9.46 GHz. For the frequency-dependent FMR measurements, a semirigid microwave cable short-circuited at its end was used [29]. These measurements were performed by sweeping the external magnetic field applied parallel to the film plane at different microwave frequencies, ranging from 2 to 26 GHz.

Element-specific magnetization dynamics of Fe and Gd sublattices in $Py_{100-x}Gd_x$ layers were measured by the TR-XRMS using the ALICE end station [22] at beamline UE56-2 at the BESSY II synchrotron radiation facility of the Helmholtz Zentrum Berlin. The time evolution of the transverse magnetization in thin ferromagnetic films after step-field pulse excitation is recorded with element selectivity at the Fe L_3 and Gd M_5 edges. The step-field excitation is performed by applying electrical pulses to the bottom Cu layer lithographically shaped to a 7×0.35 mm^2 stripline. Fast rise-time current pulses are delivered from a pulse generator and fed through the stripline, resulting in a pulsed Oersted field H_p perpendicular to the stripline (and current) direction. Electrical pulses (rise time of 0.35 ns, pulse width of 10 ns) are synchronized with the x-ray photon bunches, which have a 50-ps pulse width. Time delay scans were measured using an external bias magnetic field in the range $\mu_0 H_B = 0.8$–2.4 mT applied parallel to the stripline direction.

Femtosecond time-resolved measurements of the magneto-optical Kerr effect (TR-MOKE) were performed using p-polarized 150-fs laser pulses with a repetition rate of 260 kHz and central wavelengths of 800 nm for the probe beam and 400 nm for the pump beam. Both pump and probe pulses were applied from the film side with the angles of incidence of 55° and 45° and 200- and 100-μm spot sizes, respectively. The incident pump laser fluence was about 2 mJ/cm^2. The pump beam was modulated with an acousto-optical modulator at a frequency of 50 kHz, and the pump-induced changes in the MOKE rotation were recorded as a function of the pump-probe delay using a Wollaston prism, a balanced silicon photodiode, and a lock-in amplifier. In the case of the p-polarized probe pulse, such a detection scheme allows us to measure the appearance of the in-phase s-polarized wave (MOKE rotation, ψ_K') and the out-of-phase s-polarized wave (MOKE ellipticity, ψ_K''), proportional to the polar and longitudinal magnetization components. Since for the studied samples both MOKE rotation and ellipticity provide similar results, we will focus on the analysis of the MOKE rotation signals. An external magnetic field parallel to the plane of incidence with a magnitude of approximately 0.3 T was applied using a permanent magnet mounted on the rotation stage. It allowed us to change the angle between the film surface and the external magnetic field. Samples were cut into pieces of 3×3 and 4×4 mm^2 for the FMR and TR-MOKE measurements, respectively. All measurements were performed at room temperature (RT).

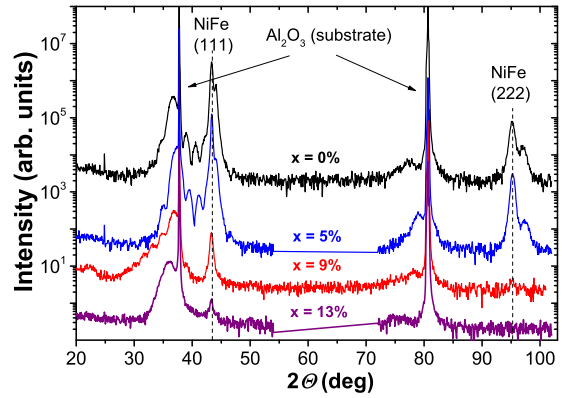

FIG. 1. XRD scans for Al_2O_3 (substrate)/Ta/Cu/$Py_{100-x}Gd_x$/Ta samples with $x = 0\%$, 5%, 9%, and 13% (from top to bottom). Scans are shifted vertically for better visibility.

III. EXPERIMENTAL RESULTS AND DISCUSSION

X-ray diffractograms of $Py_{100-x}Gd_x$ samples are shown in Fig. 1. Both the (111) and (222) peaks are present in the spectra for undoped Py and for $Py_{95}Gd_5$ films, indicating a well-defined (111)-textured fcc structure. The XRD spectra of $Py_{91}Gd_9$ and $Py_{87}Gd_{13}$ samples show a rapid reduction of the (111) peak intensity with increasing Gd concentration and no peak at the (222) position. This indicates a strong loss of crystallinity in $Py_{91}Gd_9$ and $Py_{87}Gd_{13}$ samples, leading to a polycrystalline or partially amorphous structure. The (110) and (220) reflections of the Ta-buffer layer including some Laue oscillations, which overlap the sapphire substrate peaks, are also visible.

A. Ferromagnetic resonance

Figure 2(a) shows the frequency dependence of the FMR-resonance field in the in-plane geometry for all samples. Films with larger Gd concentration exhibit larger resonance fields at identical frequencies due to the reduced anisotropy field. The latter is reduced primarily because the doping of transition-metal (TM) films by rare-earth (RE) elements like Gd, Tb, Dy, and Ho leads to a noticeable reduction in the saturation magnetization [30–34]. This leads to reduced M_{eff} as listed in Table I. The effective magnetization M_{eff} and the g factor were determined from the fit [red solid lines in Fig. 2(a)] to the experimental data points using Eq. (6).

The FMR linewidth characterizes the relaxation of the magnetization and usually has two contributions. The first one is the extrinsic frequency-independent contribution due to magnetic inhomogeneities resulting from sample imperfections and causing deviations in the internal magnetic fields (local resonance) [1,2,26]. The second one is the intrinsic contribution due to viscous damping, which is linearly proportional to the resonance frequency. The inhomogeneity contribution and the intrinsic contribution to the linewidth can be separated from the frequency dependence of the peak-to-peak linewidth ΔH_{pp} [Fig. 2(b)] using the equation [1,2,12]

$$\Delta H_{pp} = \Delta H_0 + \alpha \frac{4\pi f}{\sqrt{3}\gamma}, \tag{7}$$

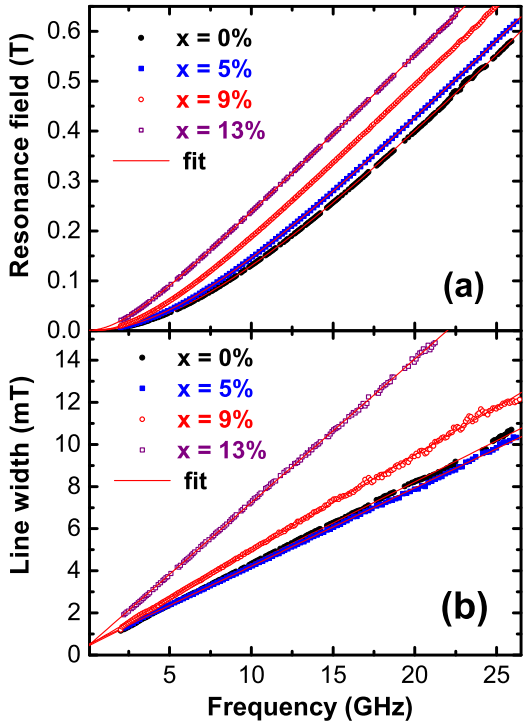

FIG. 2. Frequency dependence of the FMR (a) resonance field and (b) peak-to-peak linewidth at the magnetic field applied parallel to the $Py_{100-x}Gd_x$ film plane for different concentrations of Gd. Solid lines represent the fit.

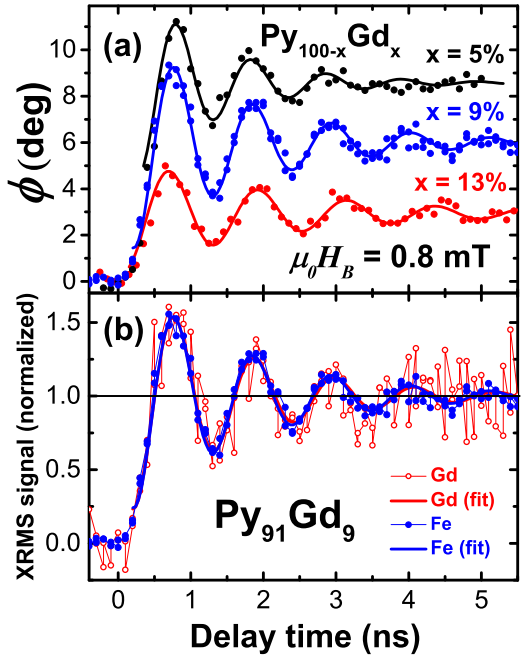

FIG. 3. (a) Precessional angle $\phi(t)$ of Fe magnetic moments as a function of the delay time after the step-pulse field excitation in $Py_{100-x}Gd_x$ thin films with $x = 5\%$, 9%, and 13% (from top to bottom). (b) Free precession of Fe (blue solid circles) and Gd (red open circles) atoms in the $Py_{91}Gd_9$ film. The value of the applied bias field for all scans is $\mu_0 H_B = 0.8$ mT. The solid lines represent the fit. All measurements are taken at room temperature.

where ΔH_0 is the term responsible for the inhomogeneous broadening. Extrapolating the linear fit in Fig. 2(b) to zero frequency, one finds that ΔH_0 is small and about 0.5 mT for all samples. We note, however, that at $f = 1$ GHz the inhomogeneous contribution is almost half of the ΔH_{pp}. The damping parameters α, determined from the fit in Fig. 2(b), are listed in Table I. The samples with a Gd concentration above 5% show a noticeable enhancement of α, which is almost twice as large in $Py_{87}Gd_{13}$ as in the Py sample. This is in line with the previously reported studies, which revealed an increase in the damping parameter by approximately a factor of 2 for $x = 10\%$ [31–34].

B. Time-resolved x-ray resonant magnetic scattering

TR-XRMS time-delay scans measured at RT for $Py_{100-x}Gd_x$ films are shown in Fig. 3(a). Circles represent the magnetization precession of Fe magnetic moments, measured at the Fe L_3 absorption edge. All scans were recorded with an external magnetic bias field of $\mu_0 H_B = 0.8$ mT applied in the film plane. The damped precessional oscillation of Fe moments is clearly seen. The precessional dynamics can be described by a solution of the LLG equation in a spherical coordinate system [23,25]:

$$\phi(t) = \phi_1 + \phi_0 \exp(-t/\tau)\sin(\omega t + \varphi_0), \tag{8}$$

where $\phi(t)$ is the in-plane angle between the magnetization and the initial state parallel to the stripline axis and ϕ_1 is the steady-state equilibrium magnetization angle after the step-field pulse excitation (rise time of 0.35 ns, pulse width of 10 ns, amplitude ~0.1 mT). In Fig. 3(a) the precessional angle $\phi(t)$ as a function of the delay time between probing photon bunches and the excitation field is plotted. The steady-state equilibrium magnetization angles ϕ_1 were obtained from the additional calibration measurements, as described elsewhere [23,25]. One can see in Fig. 3(a) that for larger x the relaxation time of magnetization precession to its new equilibrium state increases. The comparison of the decay times for all samples is presented in Table I: the decay time τ_{exp} determined by the TR-XRMS becomes larger by a factor of 2 for $Py_{87}Gd_{13}$ compared to the undoped Py. At the same time α obtained from the FMR experiments increases with Gd doping (see Table I). This counterintuitive simultaneous increase of relaxation time and Gilbert damping is explained by a significant decrease of M_{eff} upon Gd doping, as seen from the FMR measurements; see Eq. (5) for clarity.

TABLE I. Values of the effective magnetization M_{eff}, spectroscopic g factor, and dimensionless magnetic damping parameters α obtained from FMR for $Py_{100-x}Gd_x$ systems with different Gd concentrations x. The decay times τ_{calc} and τ_{exp} in $Py_{100-x}Gd_x$ alloys have been calculated from FMR data and determined from TR-XRMS experiments, respectively.

x	$\mu_0 M_{eff}$ (T)	g factor	α (10^{-3})	τ_{calc} (ns)	τ_{exp} (ns)
0	0.76 ± 0.01	2.10 ± 0.02	9.9 ± 0.1	1.4 ± 0.1	1.05 ± 0.12
5	0.61 ± 0.01	2.14 ± 0.02	9.6 ± 0.1	1.8 ± 0.1	1.1 ± 0.12
9	0.38 ± 0.01	2.17 ± 0.02	11.8 ± 0.1	2.3 ± 0.1	1.6 ± 0.15
13	0.20 ± 0.01	2.22 ± 0.02	18.2 ± 0.1	2.8 ± 0.1	2.4 ± 0.4

We have also calculated the decay time τ_{calc} for all samples, using Eq. (5) with α taken from FMR data (see Table I). The calculated values are 50% larger than the ones determined by the TR-XRMS measurements (τ_{exp} in Table I), implying that the effective damping α_{eff} probed by the TR-XRMS is larger than the intrinsic damping parameter α determined from FMR. This mismatch can be assigned to the inhomogeneous broadening (quantified by ΔH_0 in the FMR experiment), which is not taken into account in the model for the time-resolved measurements. The frequency of magnetization precession measured at the bias field of $\mu_0 H_B = 0.8$ mT is below 1 GHz. According to Fig. 2(b), the inhomogeneous contribution to the magnetic relaxation at this frequency is almost 50%. Irrespective of the quantitative discrepancy between τ_{exp} and τ_{calc}, the increase in relaxation time with the Gd concentration is evident in the set of calculated values τ_{calc}.

In Fig. 3(b) we compare the free precession of Fe and Gd magnetic moments in $Py_{91}Gd_9$ recorded at RT for $\mu_0 H_B = 0.8$ mT. Here, all data points are normalized to the x-ray intensity at the delay time, which corresponds to steady-state magnetization equilibrium [at a delay time above 5 ns in Fig. 3(b)]. One can see that within the instrumental sensitivity limit and timescale accuracy the time delay scans detected at the Fe L_3 and Gd M_5 edges coincide. Bearing in mind that magnetic moments of two magnetic sublattices are collinear and antiparallel in the magnetization equilibrium state, the match of delay scans in Fig. 3(b) indicates that the Fe and Gd magnetic moments precess in phase and with the same cone opening angle; that is, these antiferromagnetically coupled magnetic moments precess collinearly. The fits of the experimental data provide an identical exponential decay time of 1.6 ns. The observed collinear precession of the antiferromagnetically coupled sublattices at a timescale larger than 0.1 ns is expected since the noncollinear precession governed by the exchange would occur at much shorter timescales corresponding to terahertz frequencies [35].

C. Time-resolved MOKE

Figure 4 presents variations of the MOKE rotation signal measured on undoped Py ($x = 0$) for different angles of the external magnetic field with respect to the normal to the film surface. The effective magnetic field, acting on the magnetization, is a sum of the external magnetic field, the demagnetizing field, and the anisotropy field. At a negative pump-probe delay the magnetization is aligned parallel to the effective magnetic field. After the absorption of the pump pulse, the magnetic film heats up, which leads to the reduction of the magnetization and anisotropy fields, thereby altering the direction of the effective field and driving the precessional motion of the magnetization [8]. Fourier spectra of the transient MOKE signals, shown in Fig. 5, reveal excitation of the homogeneous precession of the magnetization (uniform FMR mode) and the first two nonuniform spin wave modes. The TR-MOKE data obtained for other samples look similar and demonstrate that the magnon frequencies decrease and become closer to each other with increasing Gd concentration x.

For a more detailed analysis, the experimental data were fitted with a sum of an incoherent background, reproduced according to the phenomenological model [36], and decaying

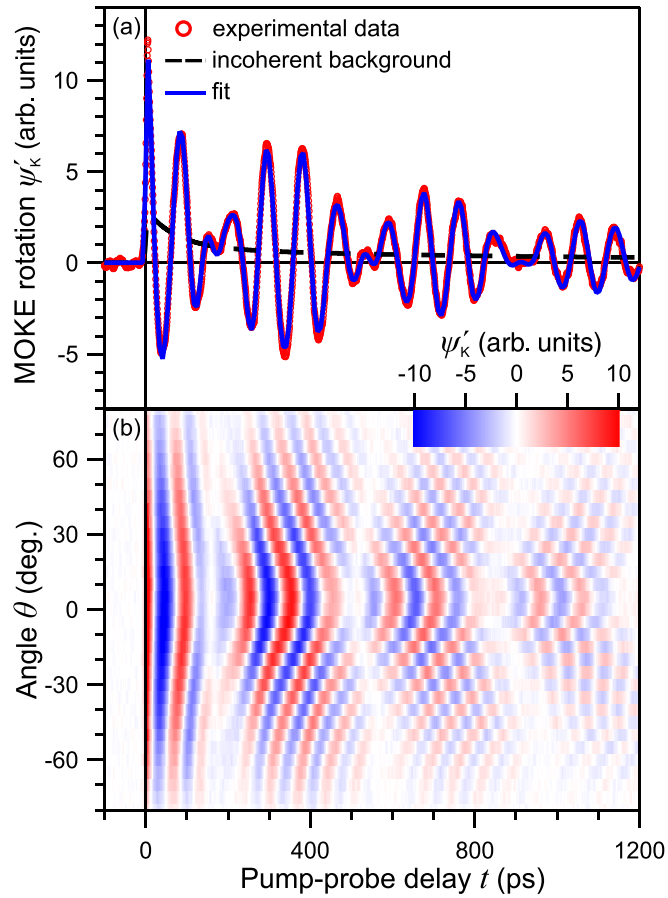

FIG. 4. Variations of the MOKE rotation signal $\psi'_K(t)$ measured on the Py sample for 40° between the normal to the film surface and the external magnetic field. The fit was performed using Eq. (9) as a fit function. (b) Two-dimensional image of the variations of the MOKE rotation signal $\psi'_K(t)$ measured on the same sample as in (a) for different pump-probe delays and angles θ between the external magnetic field and the normal to the film surface.

cosine functions:

$$\psi_K(t) = a_1 e^{-t/\tau_{i1}} + a_2(1 - e^{-t/\tau_{i1}})e^{-t/\tau_{i2}} + \sum_{n=0}^{N} m_n e^{-t/\tau_n} \cos(2\pi f_n t + \varphi_n), \quad (9)$$

where τ_{i1} and τ_{i2} are the time constants characterizing the incoherent background and τ_n, f_n, and φ_n are the lifetime, frequency, and initial phase of the magnon mode n. According to the Fourier spectra (see Fig. 5), we have to consider only the first three lowest spin wave modes ($n = 0, 1, 2$). Inspecting Figs. 4(b) and 5, one can recognize how the magnon frequencies change with the angle between the external magnetic field and the normal to the film surface. The presence of three magnon modes allows us to determine the exchange stiffness D (see Table II) as described in Refs. [7,8]. The experimental value of the exchange stiffness for an undoped Py film $D = 295 \pm 30$ meV Å^2, which corresponds to $\tilde{D} = a^3 D = (1.0 \pm 0.1) \times 10^{-11}$ J/m ($a^3 = 44.7$ Å^3 is the unit cell volume of cubic $Ni_{81}Fe_{19}$), is in a good agreement with literature values [37,38]. The exchange stiffness decreases with the increase in

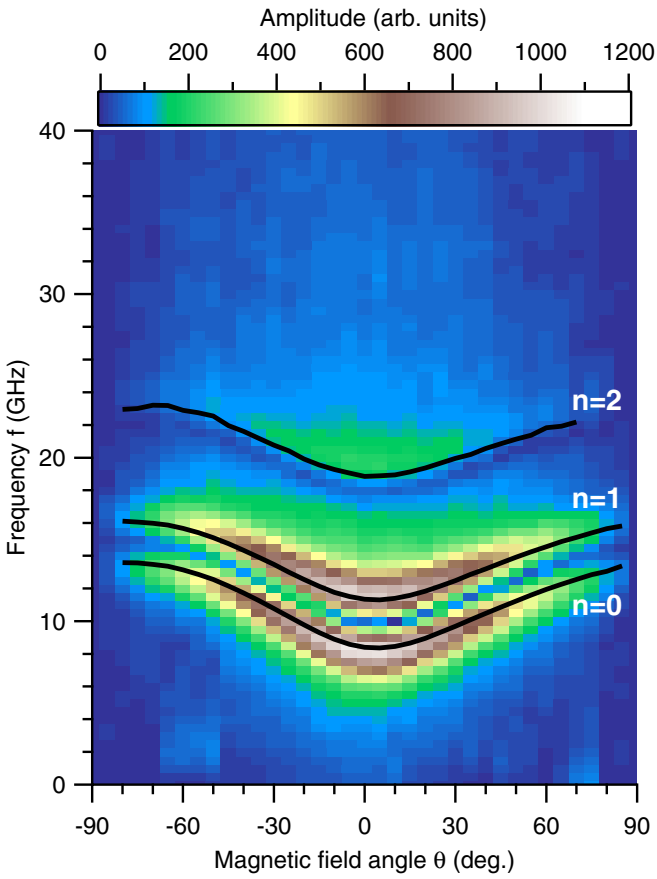

FIG. 5. Fourier spectra of the MOKE rotation measured on Py for different angles θ between the surface normal and the external magnetic field. Solid lines depict the magnon frequencies obtained in the fitting procedure of the measured MOKE signals with the sum of the decaying cosine functions [see Fig 4(a)].

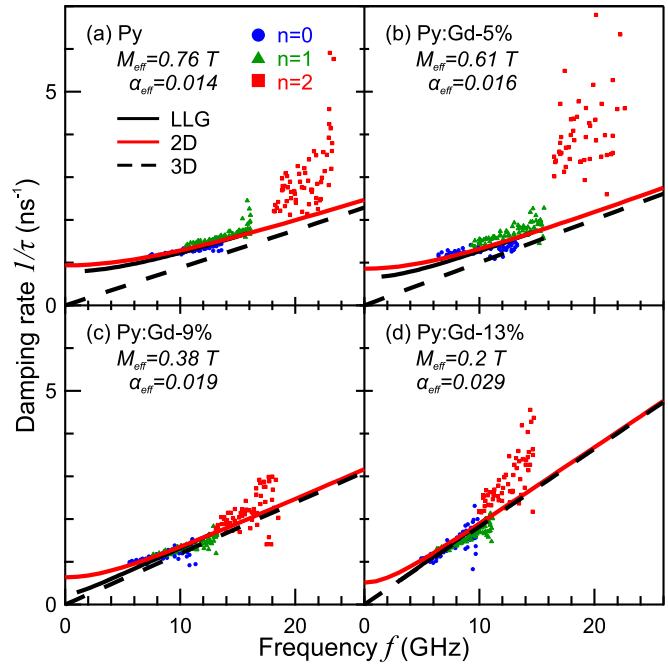

FIG. 6. Dots represent the magnon frequencies and the damping rates obtained for Al_2O_3 (substrate)/Ta/Cu/$Py_{100-x}Gd_x$/Ta structures with different Gd dopings of (a) 0%, (b) 5%, (c) 9%, and (d) 13% in the fitting procedure of the measured MOKE signals with the sum of the decaying cosine functions. Different colors and dot types correspond to different magnon modes: n = 0, blue circles; 1, green triangles; 2, red squares. Black solid lines are the results of the modeling using the LLG equation with an adjustable dimensionless damping parameter α. Solid red and black dashed lines demonstrate dependencies of the damping rate on the magnon frequency, calculated using depicted values of M_{eff} and α_{eff}, in the 2D and 3D cases, respectively.

Gd concentration, presumably due to an increase in impurity amounts and partial loss of crystallinity according to the XRD data [38].

In order to extract the dimensionless damping parameter α_{eff}, we need to analyze the dependence of the magnon relaxation rate $1/\tau$ on the magnon frequency ω, presented in Fig. 6. The experimental data corresponding to the zeroth and first magnon modes dictate linear proportionality between the damping rate and the magnon frequency, while the second magnon mode exhibits a rather nonlinear dependence. However, for all magnon modes the fitting procedure revealed systematically smaller lifetimes τ_0 (see Table II) compared to the FMR data. The fit has been performed using numerical simulations to solve the LLG equation for the zeroth and first magnon modes and corresponding orientation of the applied magnetic field with respect to the film normal.

It should be noted that the obtained numerical solutions of the LLG equations in Fig. 6 are bound by two limiting cases: collinear geometry with parallel in-plane magnetization and magnetic field described by Eq. (5) (marked as 2D in Fig. 6) and noncollinear geometry with the magnetization and magnetic field possessing out-of-plane components described by Eq. (3) (marked as 3D in Fig. 6). All curves merge together at high frequencies.

The extracted values of the Gilbert damping parameter α_{eff} slightly depend on the applied model. Thus, to extract the dimensionless damping parameter α_{eff}, we reproduced the data corresponding to the FMR and the first nonuniform spin wave mode, using the numerical solution of the LLG equation (see Fig. 6). As the main result, the modeling of the observed dynamics using the LLG equation yields ~1.6 times larger values for the parameter α_{eff}. The dependence of α on the Gd doping appears to be consistent with the results of the

TABLE II. Values of the effective magnetization M_{eff}, the spectroscopic g factor obtained from the FMR, the dimensionless effective damping parameter α_{eff}, the lifetime of the fundamental magnon mode τ_0, and the exchange stiffness D obtained from TR-MOKE measurements on $Py_{100-x}Gd_x$ systems with different Gd concentrations x.

x	$\mu_0 M_{\text{eff}}$ (T)	g	$\alpha_{\text{eff}}(\times 10^{-3})$	τ_0 (ns)	D (meV Å^2)
0	0.76	2.1	14 ± 1	0.8 ± 0.1	295 ± 30
5	0.61	2.14	16 ± 1	0.77 ± 0.10	171 ± 17
9	0.38	2.17	19 ± 2	0.85 ± 0.15	184 ± 18
13	0.2	2.22	29 ± 3	0.75 ± 0.20	106 ± 10

FMR measurements. We attribute the difference between the FMR and TR-MOKE measurements to the transient heating of ferromagnetic samples with the pump pulse, which leads to shorter lifetimes of the FMR precession, as evidenced by pump-fluence-dependent TR-MOKE measurements on permalloy thin films [39]. The possibility to measure precisely the damping of exchange magnons suggests that experiments for thinner samples, characterized by larger frequencies of exchange magnons, would allow experimental determination of the Gilbert damping over the extended frequency range.

IV. CONCLUSIONS

Using different ferromagnetic resonance techniques and probe frequencies, conventional FMR (2–26 GHz), TR-MOKE (6–23 GHz), and TR-XRMS (1 GHz), we have characterized the magnetic properties and magnetic relaxation in $Py_{100-x}Gd_x$ films with Gd concentration $x = 0\%$, 5%, 9%, and 13%. All methods reveal the increase in the g factor and decrease in the effective magnetization at larger Gd concentrations (Table I). The latter is the result of the antiferromagnetic coupling between Fe (Ni) and Gd magnetic moments. The antiferromagnetically coupled magnetic sublattices exhibit collinear precession (ferromagnetic mode [40,41]) at about 1-GHz frequency and room temperature. The increase in the Gd concentration stimulates the loss of crystallinity and decrease in the magnetic exchange stiffness as obtained from the TR-MOKE (see Table II).

All methods reveal an increase in the magnetic damping parameter in $Py_{100-x}Gd_x$ films with an increase in the Gd concentration (see Tables I and II). However, for the whole sample series the stroboscopic techniques (TR-XRMS and TR-MOKE) show larger (approximately 50%) effective damping α_{eff} compared to the intrinsic damping α derived from conventional FMR measurements. Contributions from the nonlinear effects due to larger precessional angles are unlikely in our single-pulse pump-probe methods, as has been proven in previous experimental studies [42,43]. The TR-XRMS study was performed at small magnetic fields and low resonance frequencies, where inhomogeneous contributions are significant. Thus, the sample inhomogeneity is predominantly the reason of the larger effective damping deduced from the TR-XRMS.

Spatially uniform ($n = 0$) and nonuniform ($n = 1$) magnon modes recorded using the TR-MOKE provide identical effective relaxation rates in all samples. Their ∼50% larger values compared to the FMR measurements are consistent with the pump-induced increase of the Gilbert damping parameter [39]. However, the impact of transient temperature gradients after the applied ultrashort (pump) laser pulses as well as nonlinear effects and magnon-magnon coupling on the damping parameter cannot be disentangled in our experiments. To summarize, pump-probe methods are proven to be useful in the determination of the qualitative dependence of Gilbert damping on the Gd concentration in complex magnetic alloys.

ACKNOWLEDGMENTS

The authors greatly acknowledge G. Vaudel, the research engineer on the femtosecond laser platform at the IMMM, Le Mans University, and Dr. W. Mahler at beamline UE56-2 for technical support, and Deutsche Forschungsgemeinschaft (SA3095/2-1, AL2143/2-1, and MA5144/9-1) and Agence Nationale de la Recherche for financial support under grants "Ultramox" (Grant No. ANR-14-CE26-0008), "PPMI-NANO" (Grants No. ANR-15-CE24-0032 and No. DFG SE2443/2), and Strategie internationale "NNN-Telecom" de la Region Pays de La Loire. This work is supported by BMBF 05K13PC1 and a short-term research fellowship granted to V.V.T. by the German Academic Exchange Service (DAAD). We are also thankful to the Helmholtz Zentrum Berlin for travel support under BMBF 05.ES3XBA/5. R.A. and H.Z. acknowledge the BMBF project 05K10PC2.

[1] B. Heinrich, *Spin Relaxation in Magnetic Metallic Layers and Multilayers* (Springer, New York, 2004), Vol. 3.
[2] M. Farle, Rep. Prog. Phys. **61**, 755 (1998).
[3] M. Farle, T. Silva, and G. Woltersdorf, *Spin Dynamics in the Time and Frequency Domain. Magnetic Nanostructures*, Springer Tracts in Modern Physics Vol. 246 (Springer, Berlin, 2013).
[4] B. Heinrich and J. F. Cochran, Adv. Phys. **42**, 523 (1993).
[5] R. Salikhov, L. Reichel, B. Zingsem, R. Abrudan, A. Edström, D. Thonig, J. Rusz, O. Eriksson, L. Schultz, S. Fähler, M. Farle, and U. Wiedwald, J. Phys.: Condens. Matter **29**, 275802 (2017).
[6] A. G. Gurevich and G. A. Melkov, *Magnetization Oscillations and Waves* (CRC Press, Boca Raton, FL, 1996), Vol. 1.
[7] I. Razdolski, A. Alekhin, N. Ilin, J. P. Meyburg, V. Roddatis, D. Diesing, U. Bovensiepen, and A. Melnikov, Nat. Commun. **8**, 15007 (2017).
[8] M. van Kampen, C. Jozsa, J. T. Kohlhepp, P. LeClair, L. Lagae, W. J. M. de Jonge, and B. Koopmans, Phys. Rev. Lett. **88**, 227201 (2002).
[9] F. Hellman, A. Hoffmann, Y. Tserkovnyak, G. S. D. Beach, E. E. Fullerton, C. Leighton, A. H. MacDonald, D. C. Ralph, D. A. Arena, H. A. Dürr, P. Fischer, J. Grollier, J. P. Heremans, T. Jungwirth, A. V. Kimel, B. Koopmans, I. N. Krivorotov, S. J. May, A. K. Petford-Long, J. M. Rondinelli, N. Samarth, I. K. Schuller, A. N. Slavin, M. D. Stiles, O. Tchernyshyov, A. Thiaville, and B. L. Zink, Rev. Mod. Phys. **89**, 025006 (2017).
[10] G. van der Laan, J. Electron Spectrosc. Relat. Phenom. **220**, 137 (2017).
[11] I. Neudecker, G. Woltersdorf, B. Heinrich, T. Okuno, and G. Gubbiotti, C. H. Back. J. Magn. Magn. Mater. **307**, 148 (2006).
[12] J. Lindner, K. Lenz, E. Kosubek, K. Baberschke, D. Spoddig, R. Meckenstock, J. Pelzl, Z. Frait, and D. L. Mills, Phys. Rev. B **68**, 060102 (2003).
[13] D. O. Smith, J. Appl. Phys. **29**, 264 (1958).
[14] T. J. Silva, C. S. Lee, T. M. Crawford, and C. T. Rogers, J. Appl. Phys. **85**, 7849 (1999).
[15] A. V. Kimel, A. Kirilyuk, P. A. Usachev, R. V. Pisarev, A. M. Balbashov, and Th. Rasing, Nature (London) **435**, 655 (2005).
[16] I. Radu, K. Vahaplar, C. Stamm, T. Kachel, T. Pontius, H. A. Dürr, T. A. Ostler, J. Barker, R. F. L. Evans, R. W. Chantrell,

A. Tsukamoto, A. Itoh, A. Kirilyuk, Th. Rasing, and A. V. Kimel, Nature (London) **472**, 205 (2011).

[17] T. A. Ostler, J. Barker, R. F. L. Evans, R. W. Chantrell, U. Atxitia, O. Chubykalo-Fesenko, S. El Moussaoui, L. Le Guyader, E. Mengotti, L. J. Heydermann, F. Nolting, A. Tsukamoto, A. Itoh, D. Afanasiev, B. A. Ivanov, A. M. Kalashnikova, K. Vahaplar, J. Mentink, A. Kirilyuk, Th. Rasing, and A. V. Kimel, Nat. Commun. **3**, 666 (2012).

[18] J. Walowski and M. Münzenberg, J. Appl. Phys. **120**, 140901 (2016).

[19] B. Koopmans, J. J. M. Ruigrok, F. DallaLonga, and W. J. M. de Jonge, Phys. Rev. Lett. **95**, 267207 (2005).

[20] M. O. A. Ellis, T. A. Ostler, and R. W. Chantrell, Phys. Rev. B **86**, 174418 (2012).

[21] N. Kazantseva, U. Nowak, R. W. Chantrell, J. Hohfeld, and A. Rebei, Europhys. Lett. **81**, 27004 (2008).

[22] R. Abrudan, F. Brüssing, R. Salikhov, J. Meermann, L. Le Guyader, H. Ryll, I. Radu, F. Radu, and H. Zabel, Rev. Sci. Instrum. **86**, 063902 (2015).

[23] St. Buschhorn, F. Brüssing, R. Abrudan, and H. Zabel, J. Phys. D **44**, 165001 (2011).

[24] R. Salikhov, R. Abrudan, F. Brüssing, K. Gross, C. Luo, K. Westerholt, H. Zabel, F. Radu, and I. A. Garifullin, Phys. Rev. B **86**, 144422 (2012).

[25] W. E. Bailey, L. Cheng, D. J. Keavney, C.-C. Kao, E. Vescovo, and D. A. Arena, Phys. Rev. B **70**, 172403 (2004).

[26] R. D. McMichael, D. J. Twisselmann, and A. Kunz, Phys. Rev. Lett. **90**, 227601 (2003).

[27] S. Buschhorn, F. Brüssing, M. Ewerlin, R. Salikhov, R. Abrudan, and H. Zabel, J. Appl. Phys. **112**, 103914 (2012).

[28] R. Salikhov, F. Brüssing, K. Gross, F. Radu, R. Abrudan, and H. Zabel, Phys. Status Solidi B **253**, 1782 (2016).

[29] F. M. Römer, M. Möller, K. Wagner, L. Gathmann, R. Narkowicz, H. Zähres, B. R. Salles, P. Torelli, R. Meckenstock, J. Lindner, and M. Farle, Appl. Phys. Lett. **100**, 092402 (2012).

[30] I. Radu, G. Woltersdorf, M. Kiessling, A. Melnikov, U. Bovensiepen, J.-U. Thiele, and C. H. Back, Phys. Rev. Lett. **102**, 117201 (2009).

[31] G. Woltersdorf, M. Kiessling, G. Meyer, J.-U. Thiele, and C. H. Back, Phys. Rev. Lett. **102**, 257602 (2009).

[32] W. Bailey, P. Kabos, F. Mancoff, and S. Russek, IEEE Trans. Magn. **37**, 1749 (2001).

[33] S. E. Russek, P. Kabos, R. D. McMichael, C. G. Lee, W. E. Bailey, R. Ewasko, and S. C. Sanders, J. Appl. Phys. **91**, 8659 (2002).

[34] Y. Fu, L. Sun, J. Wang, X. Bai, Z. Kou, Y. Zhai, J. Du, J. Wu, Y. Xu, H. Lu, and H. Zhai, IEEE Trans. Magn. **45**, 4004 (2009).

[35] S. Parchenko, T. Satoh, I. Yoshimine *et al.*, Appl. Phys. Lett. **108**, 032404 (2016).

[36] N. Del Fatti, C. Voisin, M. Achermann, S. Tzortzakis, D. Christofilos, and F. Valleé, Phys. Rev. B **61**, 16956 (2000).

[37] R. K. Dumas, E. Iacocca, S. Bonetti, S. R. Sani, S. M. Mohseni, A. Eklund, J. Persson, O. Heinonen, and J. Akerman, Phys. Rev. Lett. **110**, 257202 (2013).

[38] J. Wei, Z. Zhu, C. Song, H. Feng, P. Jing, X. Wang, Q. Liu, and J. Wang, J. Phys. D **49**, 265002 (2016).

[39] S. Mondal and A. Barman, Phys. Rev. Appl. **10**, 054037 (2018).

[40] F. Schlickeiser, U. Atxitia, S. Wienholdt, D. Hinzke, O. Chubykalo-Fesenko, and U. Nowak, Phys. Rev. B **86**, 214416 (2012).

[41] J. Kaplan and C. Kittel, J. Chem. Phys. **21**, 760 (1953).

[42] J. P. Nibarger, R. Lopusnik, and J. Silva, Appl. Phys. Lett. **82**, 2112 (2003).

[43] Th. Gerrits, M. L. Schneider, A. B. Kos, and T. J. Silva, Phys. Rev. B **73**, 094454 (2006).